

## Article

# Machine Learning-Based Prediction of Node Localization Accuracy in IIoT-Based MI-UWSNs and Design of a TD Coil for Omnidirectional Communication

Qiao Gang <sup>1,2,3</sup>, Aman Muhammad <sup>1,2,3,\*</sup> , Zahid Ullah Khan <sup>1,2,3</sup>, Muhammad Shahbaz Khan <sup>4</sup> , Fawad Ahmed <sup>5</sup> and Jawad Ahmad <sup>6</sup> 

<sup>1</sup> Acoustic Science and Technology Laboratory, Harbin Engineering University, Harbin 150001, China

<sup>2</sup> Key Laboratory of Marine Information Acquisition and Security, Harbin Engineering University, Ministry of Industry and Information Technology, Harbin 150001, China

<sup>3</sup> College of Underwater Acoustic Engineering, Harbin Engineering University, Harbin 150001, China

<sup>4</sup> Department of Electrical Engineering, Heavy Industries Taxila Education City (HITEC) University, Taxila 47080, Pakistan

<sup>5</sup> Department of Cyber Security, Pakistan Navy Engineering College, National University of Science and Technology (NUST), Karachi 75350, Pakistan

<sup>6</sup> School of Computing, Edinburgh Napier University, Edinburgh EH10 5DT, UK

\* Correspondence: aman@hrbeu.edu.cn

**Abstract:** This study aims to realize Sustainable Development Goals (SDGs), i.e., SDG 9: Industry Innovation and Infrastructure and SDG 14: Life below Water, through the improvement of localization estimation accuracy in magneto-inductive underwater wireless sensor networks (MI-UWSNs). The accurate localization of sensor nodes in MI communication can effectively be utilized for industrial IoT applications, e.g., underwater gas and oil pipeline monitoring, and in other important underwater IoT applications, e.g., smart monitoring of sea animals, etc. The most-feasible technology for medium- and short-range communication in IIoT-based UWSNs is MI communication. To improve underwater communication, this paper presents a machine learning-based prediction of localization estimation accuracy of randomly deployed sensor Rx nodes through anchor Tx nodes in the MI-UWSNs. For the training of ML models, extensive simulations have been performed to create two separate datasets for the two configurations of excitation current provided to the Tri-directional (TD) coils, i.e., configuration1-case1\_configuration2-case1 (c1c1\_c2c1) and configuration1-case2\_configuration2-case2 (c1c2\_c2c2). Two ML models have been created for each case. The accuracies of both models lie between 95% and 97%. The prediction results have been validated by both the test dataset and verified simulation results. The other important contribution of this paper is the development of a novel assembling technique of a MI-TD coil to achieve an approximate omnidirectional magnetic flux around the communicating coils, which, in turn, will improve the localization accuracy of the Rx nodes in IIoT-based MI-UWSNs.

**Keywords:** localization; magneto inductive communication; underwater wireless sensor networks; machine learning; linear regression; ultrareliable low latency communication



**Citation:** Gang, Q.; Muhammad, A.; Khan, Z.U.; Khan, M.S.; Ahmed, F.; Ahmad, J. Machine Learning-Based Prediction of Node Localization Accuracy in IIoT-Based MI-UWSNs and Design of a TD Coil for Omnidirectional Communication. *Sustainability* **2022**, *14*, 9683. <https://doi.org/10.3390/su14159683>

Academic Editor: Mirco Peron

Received: 22 June 2022

Accepted: 4 August 2022

Published: 6 August 2022

**Publisher's Note:** MDPI stays neutral with regard to jurisdictional claims in published maps and institutional affiliations.



**Copyright:** © 2022 by the authors. Licensee MDPI, Basel, Switzerland. This article is an open access article distributed under the terms and conditions of the Creative Commons Attribution (CC BY) license (<https://creativecommons.org/licenses/by/4.0/>).

## 1. Introduction

The industry and academia have been collaborating for a while to realize the Sustainable Development Goals (SDGs) set by the United Nations to focus on sustainable methods of underwater communication. They intend to make it more energy-efficient [1], robust, and safe for marine life. Furthermore, the new techniques in underwater communication should also cater to the future applications in the industrial internet-of-things (IIoT) and underwater wireless sensor networks (UWSNs). Recently, wireless sensor networks (WSNs) and IIoT technologies emerged as a part of modern communication applications [2]. Many researchers are focusing on the performance improvement of UWSNs, particularly through

localization of nodes. The UWSNs eliminate the risks associated with cable structures and make the monitoring applications less complicated and quite efficient [3,4]. By utilizing node localization in UWSNs, different locations can be detected and measured remotely to obtain real-time sensor node data, and these data may further be stored at various locations at a lower cost [5]. Furthermore, the sensors may further be connected to efficient microcontroller units (MCUs), which may statistically process the data to create a complete underwater monitoring system. Such monitoring systems can effectively be utilized for marine life monitoring applications.

MI communication is quite robust and has the potential to be implemented in the industrial internet-of-things (IIoT) applications, especially for UWSNs. MI communication is the most preferable mode of communication for medium- and short-range communication. In addition to being robust (which is preferable for IIoT applications, e.g., underwater gas and oil pipeline monitoring), it is also safe for marine life. Presently, the preferred modes of underwater communication are acoustic and sonar, which majorly affect marine life communication, e.g., dolphins, whales, etc. Additionally, autonomous underwater vehicles (AUVs) also use sonar and acoustics for their communication; due to being in close contact with the marine life, the marine life communication may be affected. MI communication, on the other hand, does not affect natural underwater species' communication. Hence, MI communication tends to be a most feasible technology for manmade underwater communication systems, e.g., the AUVs, UWSNs, etc.

This study focuses on two SDGs, i.e., SDG 9: Industry Innovation and Infrastructure and SDG 14: Life below Water through the improvement of node localization estimation accuracy in MI-UWSNs. The accurate localization of sensor nodes in MI communication can effectively be utilized for industrial IoT applications, e.g., underwater gas and oil pipeline monitoring [6], and, also, in other important underwater applications, e.g., smart monitoring of sea animals [7–10], etc. Moreover, as this work is based on MI communication, it can potentially be utilized for safe communication between autonomous underwater vehicles without effecting sea life. Furthermore, UWSNs hold importance in several IIoT applications, such as in military and defense applications, e.g., to detect potential adversaries in ports, for port monitoring and control [11], in finding marine mines [12], in water border security against illegal fighter ships [13], etc. Furthermore, modern UWSN technology, such as mobile UWSNs, provides warning notifications ahead of natural calamities, such as seismic and seabed events [14]. Hence, UWSNs hold potential importance in IIoT applications.

As described earlier, the most feasible technology for medium- and short-range communication in IIoT-based UWSNs is MI communication, because, in several underwater applications, the organic materials, such as oil, gas, soil, minerals, etc., tend to attenuate the acoustic and electromagnetic signals. In contrary, the MI communication does not get affected due to the presence of organic materials [15–17] and, hence, can be used to accurately localize sensor Rx nodes in underwater and underground habitats. Therefore, the performance of the MI-UWSNs in IIoT/IoT applications strongly depends on the localization estimation accuracy of the deployed sensor Rx Nodes. Hence, it is critically important to correctly estimate the localization accuracy. Moreover, in the design process and testing of the tri-dimensional coils, the localization accuracies are used and play an indispensable role. These accuracy values are conventionally obtained after tedious simulations and experimentation, which usually take multiple hours. Subsequently, the design process takes a lot of time and effort just to obtain the accuracy values. Therefore, there is an indispensable need to intelligently automate the accuracy prediction process using artificial intelligence. Moreover, in artificial intelligence, the machine learning methods have been playing a potential role in predicting the accuracies for various applications [18,19]. This paper presents a machine learning-based prediction of the localization accuracy of randomly deployed sensor Rx nodes through anchor Tx nodes in MI-UWSNs.

The key contributions of this paper are:

- The formulation of datasets after extensive simulations of defined configurations and cases. Currently, there is nearly no publicly available localization dataset for MI communication between anchor Tx and sensor Rx nodes.
- Machine learning-based predictions of the localization estimation accuracy of randomly deployed Rx sensor nodes.
- Development of a novel assembling technique of MI-TD coil to achieve an approximate omnidirectional magnetic flux around the communicating coils, which, in turn, will improve the localization accuracy with less resources in MI-UWSNs. Due to this, localization can be done with a lesser number of anchor nodes, resulting in less energy consumption, which is critically important for IIoT applications.

The rest of the paper is structured as follows. Section 2 presents the related works containing the latest and organized literature related to the work presented in this paper. Section 3 presents the preliminaries, including the basics of node localization and the requisite details of two cases of magneto-inductive communication, from which the dataset has been formulated. Section 4 entails the machine learning prediction of the accuracy of the localization estimation in MI-UWSNs, whereas Section 5 presents a new TD coil configuration to achieve an approximate omnidirectional magnetic flux around the communicating coils. Moreover, Section 6 presents the comparison and summary of old and improved localization accuracies, followed by a concise conclusion in Section 7.

## 2. Related Work

Niaz *et al.* in [20,21] worked on creating a set of low-cost multi-coil structures that can serve as potential transmission Tx and receiver Rx nodes in MI wireless sensor networks (MI-WSNs). Their main goal was to improve the MI communication pattern, which is formed in response to the current applied to each individual coil in a TD coil configuration. They opted three different configurations for applying the current to the coils. In the first configuration, the excitation current was applied simultaneously, because all the three coils were connected in series. In the second configuration they connected each coil to a separate excitation source. However, in the third configuration, every coil was a separate entity, where the excitation current was provided sequentially by using a switch. They claimed that the third configuration was more optimal to use, because the magnetic field generated as an output to the applied excitation current, was covering a large area for communication. On the other hand, the first and second configurations had large blind areas where no communication was possible.

Gaoding *et al.* in [22] proposed and also analyzed two modes of operations for MI coils. The first one was based on a static quasi-approach, and the second was a dynamic rotation magnetic coupling. They set each of the three coils  $120^\circ$  apart in their proposed TD coil configuration. Their work shows promising results in achieving a fairly improved communication pattern of magnetic flux around the TD coils. However, the main flaw in their setup was, as long as the phase of the excitation current was kept the same, they were having good MI communication patterns, but with a slight difference in the phase of the applied excitation current to the TD coil, they suddenly lost the near- to omnidirectionality pattern of the MI communication. They were able to achieve a communication distance of 10 m with a path loss between  $-80$  and  $-150$  dB.

Muzzammil and Bai *et al.* in [23,24] investigated a relaying technique to increase the communication distance of two MI nodes. They called the opted technique active relaying. This active relaying is established by putting coils that are connected to a capacitor in a series between the communicating Tx and Rx nodes. The presence of the capacitor enables the coils to achieve a resonance phenomenon, which was the key to establishing a communication link for long distances in MI communication. They mention that this method will be best suitable for monitoring purposes of underwater and underground static structures, i.e., base of a bridge, an oil pipeline from offshore to onshore oil supply, or waste water canals and pipelines under urban areas. They mention that their system will be able to quantify any kind of major movement in the aforementioned structures.

Qiao *et al.* in [25] addressed the effect of directionality on the localization of sensor Rx nodes in MI-UWSNs. Their study was based on [20,21], where they divided the discussed TD coils configuration into a further two cases, i.e., configuration 1 case1 (c1c1), configuration 1 case 2 (c1c2) and configuration 2 case1 (c2c1), configuration 2 case 2 (c2c2). In these four newly discussed cases, they first quantify the error caused by the blind areas in MI communication. Then, they incorporate the error in a multilateration-based localization algorithm to realize how much inaccuracy the MI communication will face due to blind areas when it will be deployed in real-life scenarios. In their study, the method they opted to localize nodes with, consists of two steps. At first, they calculate the Euclidian distances between the Tx and Rx nodes. Once the distance is calculated, then the minimum of the functions is calculated with the gauss newton method.

Singh *et al.* in [26] proposed a method that can predict the average localization accuracy in wireless sensor networks (WSNs). They used a support vector machine (SVM)-based method and called their opted process as support vector regression (SVR), which they further divided into three subcategories. The three subcategories are built on features information standardization to estimate the average node localization accuracy quickly and accurately.

Lynn *et al.* in [27] used a linear regression-based algorithm to estimate the localization accuracy of sensor nodes using the time difference of arrival (TDOA) technique in underwater acoustical wireless sensor networks (UAWSNs). They first track the position/location of mobile and stationary nodes by using the approximate maximum likelihood algorithm. Their opted method reduced the median distance inaccuracy from 71% to 50% for stationary nodes and to 34% for mobile nodes. The median distance of the in-depth accuracy has also been improved from 0.49 to 0.04 m. The aforementioned study was done to track salmon passage in a dam on the Snake River in Washington USA.

Gong *et al.* in [28] analyzed an autodetection machine learning-based localization scheme for UAWSNs. They used a linear frequency modulated (LFM) for the purpose of detecting the targets position and velocity. By employing TDOA, they suggested that to successfully analyze the signal's spectrum. A fractional Fourier transform (FrFT) can be used to find the radial velocity and location of the target under observation. One important factor they mention was, by using smaller samples, the accuracy of the target location can be improved, but this will also increase the complexity of the system. Therefore, to overcome the issue of total internal complexity of the localization system, they opted oversampling of the area where the peaks of the energy spread spectrum were observed. This way, they were able to increase the accuracy of the overall system, and the issue of complexity was also catered automatically.

Chen *et al.* in [29] divided the simulation environment into smaller but equal sections, where they emphasized the fact that a machine learning algorithm if deployed for evaluating the localization accuracy of a sensor Rx node. It must first be trained on the known location of the beacon nodes. Therefore, through this approach, a one-against-one SVM-based location algorithm can be deployed to perform the aforementioned task. They tested their designed model for both range-free and range-based observations. Collectively, this model was called support vector machine one against one location algorithm (SOAOLA).

After going through a lot of work by different research groups, some of which are briefly discussed above. Our research group found out two points that no one had catered to until this day. The first one is that there are different studies on the machine learning-based localization estimation accuracy of sensor Rx nodes in WSNs, but none of the study had been done for MI-UWSNs. Secondly, no study had been conducted on the possibility to improve the directivity pattern of the magnetic flux around the TD coils to make it a near to possible omnidirectional. Therefore, in our study, we will be focusing on both the aforementioned points, where we will try our best to analyze all the factor that can make the localization of sensor Rx nodes based on MI communication predictable.

### 3. Preliminaries

This section entails the basics of node localization for the ease of readers. This section also contains the requisite details of two cases of magneto-inductive communication from which the dataset was formulated. This dataset was obtained after extensive experimentation at Harbin Engineering University (Underwater Acoustics Engineering Department) and has already been published [25]. In this paper, this dataset was used for the training, validation, and testing of the machine learning model.

#### 3.1. Node Localization

The key components in localization of a node in UWSNs are sensor Rx nodes and anchor Tx nodes. Sensor Rx nodes are the one whose location is not known and are to be localized; in some studies, they are also referred to as receiving Rx nodes. Anchor Tx nodes are the ones whose locations are already known; they are also called transmitting Tx nodes in some studies. A basic localization query is defined as determining or predicting the position of a point of interest in a two-dimensional (2D) or three-dimensional (3D) space inside a coordinate system that is generated by using known references. In general, a node's localization is estimated by taking into account movement from a known node's position, which implies some inertial and directional predictions. To localize nodes in UWSNs, we take into account all the possible devices with communication capabilities that contribute to the location estimation procedure in some way. Greenwich is used as our equatorial reference point to specify a specific location on Earth [30,31]. In some cases, this globally accepted reference coordinates are useful, but in others, we need some regional references that are important locally [32]. As a result, we need a translation system that can describe reference position points for a particular application, such as traveling, surveillance, mining, military application, community settlement planning, etc. Advanced sensor node position estimation algorithms in UWSNs rely on basic datasets, such as distance and observable angles. That can be derived intuitively from a variety of factors, namely arrival times, arrival time differences, arrival time field strength, phase variations, and phase differences [33–37]. New technologies have aided the faster gathering of location-related variables and have also improved the reliability [38].

Underwater positioning systems that are used in submarine/AUV for their own position estimation in UWSNs also require the aid of new technologies relating to terrestrial localization of a node in WSNs. Acoustic technology is, without a doubt, the most widely utilized, investigated, and well-established in UWSNs. However, due to the high cost of acoustical communication equipment, it is not feasible to use acoustic communication for the localization of Rx nodes in UWSNs when considering the medium and near fields of communication. Two technologies mainly exist for medium and near-field communication in UWSNs, i.e., VLC and MI communication [39,40]. In this study, we will be focusing on the use of MI communication technology in UWSNs [41,42]. The goal of localization is to determine the exact location of a concern node with no estimation errors. However, because of economic constraints, it is widely acknowledged that such a goal will never be achieved. As we all know, location is always linked to a reference point, which, in the most basic model, might be a list of well-known positions. However, it must be remembered that geographic locations are frequently subject to error margins. Inaccuracy might also be caused by equipment malfunctions. Electronic or quantum noise can also cause errors in the readings that are obtained by the electrical components, and variations in component specifications from different manufacturers can also be a cause. Secondly, we cannot use all the resources that we have in one go to approach an existing problem that, in our case, will be localization of a sensor Rx node in UWSNs. Therefore, it is a dire need of the time to adapt some machine learning algorithm that can predict the accuracy of the localization of sensor Rx nodes before even deploying in the network itself.

Significant sources of uncertainty in UWSNs node's localization are linked to signal propagation occurrences such as reflection, refraction, absorption, and diffraction. That can affect measurements to deviate significantly from the ideally desired value. They are

frequently regarded as random variables, and statistical models are used to characterize them. Due to the type of material and topology of the transmission medium, all of the variables affecting the accuracy of the localization can vary. It is important to note that, in UWSNs, the mobility pattern of anchor nodes causes variations in propagation parameters. That results in uneven yet site-dependent location inaccuracies.

### 3.2. Localization Accuracy Values from Experimentation

The physical nature of the magnetic field lines created by applying an excitation current to TD coils used for communication in MI-UWSNs is a complex concept to grasp because of the blind areas. Blind areas are those spots in the communication radius where no communication took place. These blind areas were discussed/analyzed/and incorporated in a multilateration-based localization algorithm in our previous study [25] that was recently published, where we have localized sensor Rx nodes with the help of anchor Tx nodes in a 15 m × 15 m simulation environment created on MATLAB. The accuracy of our opted localization algorithm for different configurations is given in Table 1.

**Table 1.** Localization estimation accuracy results.

S. No	Number of Tx Nodes	1 Rx Node	2 Rx Node	3 Rx Node	4 Rx Node	5 Rx Node	6 Rx Node	7 Rx Node	8 Rx Node	9 Rx Node	10 Rx Node
1	2Tx nodes ((C_1C_1)(C_2C_1))	90.26%	89.4%	88.2%	86.8%	83.33%	81.66%	80.13%	79.2%	77.3%	76.86%
2	2Tx nodes (C_1C_2)	65.3%	64.6%	61.67%	60.73%	59%	56.26%	53.66%	52.86%	52.2%	51.6%
3	2Tx nodes (C_2C_2)	78.6%	77.6%	76.26%	75%	73.73%	72.46%	70.93%	72.2%	66.6%	64.86%
4	3Tx nodes ((C_1C_1)(C_2C_1))	93.26%	91.8%	91%	90.73%	90.06%	88.3%	87.4%	87%	86.53%	85.8%
5	3Tx nodes (C_1C_2)	78.6%	77.5%	76.86%	76.06%	75%	74.2%	71.6%	69.6%	68.13%	66.8%
6	3Tx nodes (C_2C_2)	82%	84.73%	83.6%	83.26%	82.46%	81.6%	80.73%	80.26%	79.93%	79.13%
7	4Tx nodes ((C_1C_1)(C_2C_1))	96.53%	96.26%	96.06%	95.8%	95.6%	95.4%	95.26%	95.2%	95.06%	94.93%
8	4Tx nodes (C_1C_2)	84.6%	84.2%	83.6%	80.46%	79.13%	76.26%	74.73%	73.53%	72.6%	71.73%
9	4Tx nodes (C_2C_2)	88.6%	87.26%	86%	84%	82%	8.53%	79.13%	78.26%	77.53%	77.3%
10	8Tx nodes ((C_1C_1)(C_2C_1))	99.2%	98.86%	98.6%	98.26%	98.06%	97.93%	97.73%	97.6%	97.53%	97.46%
11	8Tx nodes (C_1C_2)	89.53%	89.13%	88.6%	87.86%	84.86%	82.93%	80.93%	80.06%	78.46%	77.06%
12	8Tx nodes (C_2C_2)	90.04%	89.93%	89.53%	89.2%	88.6%	88.06%	87.86%	87.46%	87.26%	87.13%

The main purpose of this study is to create a machine learning-based technique that can predict the localization accuracy of sensor Rx nodes prior to their deployment in the localization environment, which will save both time and resources. Completing the task of predicting the localization accuracy by clustering and classification seems superficial to us, so we used a linear regression-based machines learning technique, which is the best fit to address this kind of a problem.

## 4. Machine Learning-Based Prediction of Localization Accuracies

### 4.1. Dataset Formulation

Before moving into the actual process of localization through machine learning, the dataset needs to be formulated, which will be used for training, validation, and testing of the model. No dataset related to node localization accuracies was publicly available online; therefore, we created a dataset from extensive experimentation at the College of Underwater Acoustics Engineering, Harbin Engineering University. The results of these experiments have already been published in [25].

The created dataset was the result of simulations performed on MATLAB, where a minimum of 1 and a maximum of 10 sensor Rx nodes are localized with the help of minimum 2 and maximum 10 anchor Tx nodes. For every iteration, the sensor Rx nodes were randomly distributed in the 15 m × 15 m realm. The whole dataset is the result

of 600 iterations, which were performed separately one by one at a time. Creating this dataset was the most hectic part of this study, which took a lot of resource and time to create. The dataset was divided into two cases. First, the dataset that we created regards configuration 1 case1 (c1c1) and configuration 2 case 1 (c2c1). Both c1c1 and c2c1 depict the omnidirectionality, as shown in Figures 1b and 2b. The second dataset, on the other hand, is regarding the configuration 1 case 2 (c1c2) and configuration 2 case 2 (c2c2). Here, both c1c2 and c2c2 have different communication blind areas, which are responsible for dropping the accuracy of the localization algorithm shown in Figures 1c and 2c, respectively.

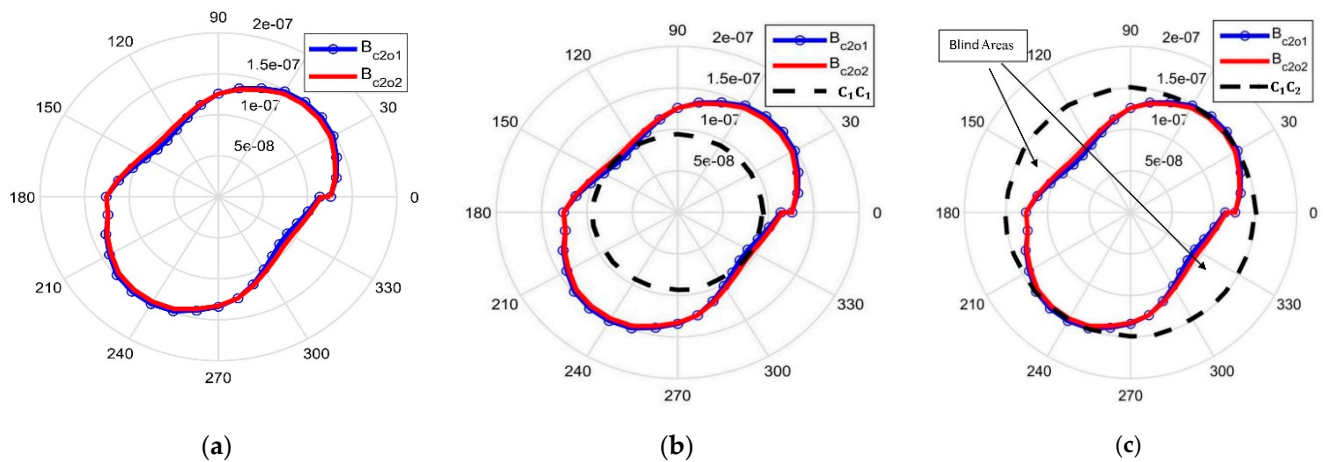


**Figure 1.** Max flux density of the magnetic fields and its directivity pattern calculated at the  $xy$  plane, and keeping the  $z = 1$  m, coil radius of transmitter Tx, and receiver Rx = 0.104 m; turns of the coil are  $N = 28$ , current  $I = 1.62 \times 10^{-7}$ , and frequency  $f = 125$  KHZ. (a) Configuration 1. (b) Configuration 1 Case 1. (c) Configuration 1 Case 2.

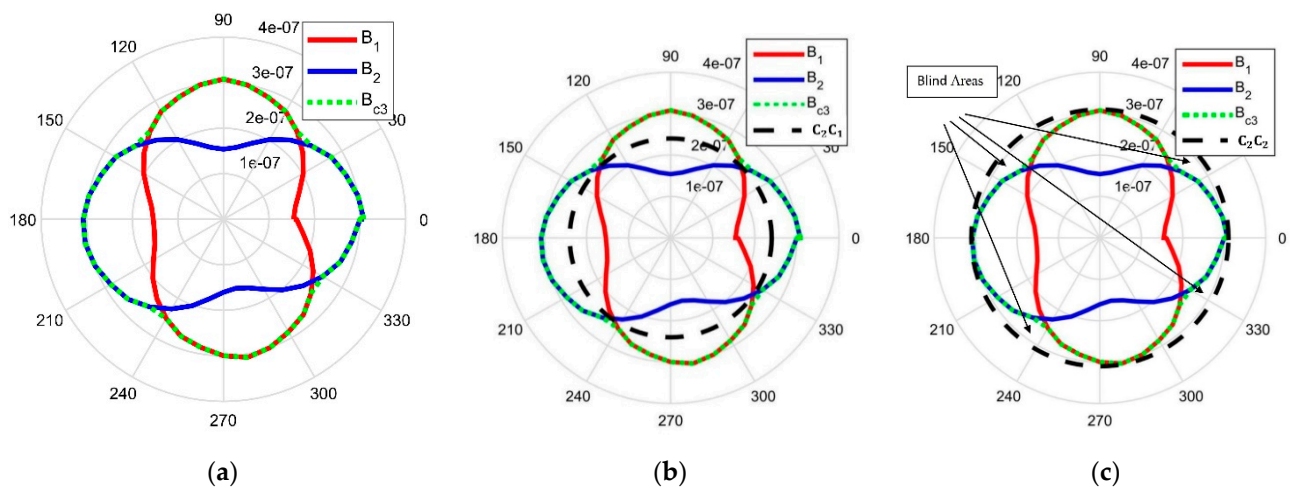


**Figure 2.** Max flux density of the magnetic fields and its directivity pattern calculated at the  $xy$  plane, and keeping the  $z = 1$  m, coil radius of transmitter Tx and receiver Rx = 0.104 m; turns of the coil are  $N = 28$ , current  $I = 1.62 \times 10^{-7}$ , and frequency  $f = 125$  KHZ. (a) Configuration 2. (b) Configuration 2 case 1. (c) Configuration 2 case 2.

In the created dataset, all the localization estimation accuracies are dependent variables. The increase or decrease in the number of sensor Rx and anchor Tx nodes is our independent variable. Reason for the dependent and independent categorization of variables in our dataset is that, the localization estimation accuracy changes with the change in the number of the Rx and Tx nodes. However, each iteration is independent of each other's output; therefore, they were considered as independent features in our created/used datasets.

These datasets were used for the prediction of localization accuracy in MI-UWSNs. Outline of the used datasets is provided in Table 2.

Table 2. Outline of the MI datasets.

S. No	Datasets Names	Total Features	Dependent Features Y	Independent Features X	Num of Anchor Tx Nodes	Num of Sensor Rx Nodes	Signal Strength
1	c1c1c2c1	10	4	6	Min 2 ... .. Max 8	Min 1 ... .. Max 10	55 dB ... .75 dB
2	c1c2c2c2	14	8	6	Min 2 ... .. Max 8	Min 1 ... .. Max 10	55 dB ... .75 dB
3	Magnetic flux along x-axis (Hx)	8	1	7	Min 2 ... .. Max 8	Min 1 ... .. Max 10	55 dB ... .75 dB
4	Magnetic flux along y-axis (Hy)	8	1	7	Min 2 ... .. Max 8	Min 1 ... .. Max 10	55 dB ... .75 dB
5	Magnetic flux along z-axis (Hz)	8	1	7	Min 2 ... .. Max 8	Min 1 ... .. Max 10	55 dB ... .75 dB

The dataset utilized in this study is verified [25] and has been obtained after extensive experimentation. The formulated dataset has a 70:30 split ratio, i.e., 70% data is used for ‘training + validation’ and the remaining 30% for the ‘testing’ of the model. The ‘training+validation’ data has further been split into 70:30, i.e., 70% for the training and 30% for the validation. Furthermore, there was no overlapping in the test dataset, i.e., it was not included in the training data. The details of dataset splitting are given in Table 3 and Figure 3.

Table 3. MI Dataset.

	Case 1 (c1c1, c2c1)	Case 2 (c1c2)	Case 2 (c2c2)	Total
Training + validation samples	140	140	140	420
Test samples	60	60	60	180
Total samples	200	200	200	600

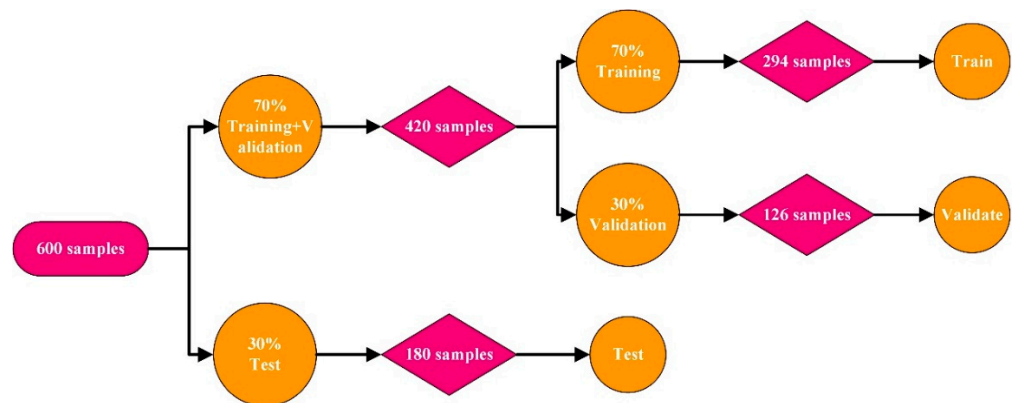


Figure 3. A flow diagram elaborating the distribution of the samples throughout the prediction of localization estimation accuracy.

#### 4.2. Prediction of Localization Accuracy for the c1c1, c2c1 Cases

A linear regression-based machine learning technique is used to predict the localization estimation accuracy of sensor Rx nodes while considering case 1 of both configurations 1 and 2. If we see the c1c1 and c2c1 from Figures 1b and 2b, it is observed that, by considering the aforementioned cases, same omnidirectional behavior of communication in MI-UWSNs is repeated. That is why it is assumed that the localization estimation accuracy prediction results for both the configurations will also be the same. Therefore, by keeping this assumption that is based on our previous study in [25], there will be less dependent variables in the dataset provided for prediction, which, in turn, will require less time to process.

The process of prediction as a pseudo code is shown as Algorithm 1. This whole process was done in python. At the first step, all the libraries regarding the procedure were

loaded. Then, we loaded the data by which the model is first trained, validated, and then the same data was used to test our model. We used a 70/30 configuration, which means that 70 percent of the data is used to train and validate the model, and 30 percent of the data is used to test the model, as shown in Table 3. Moreover, for a better understanding, the distribution of the samples in the used MI dataset can be seen in Figure 3.

---

**Algorithm 1:** A Pseudo Code of the Prediction Process for c1c1c2c1.

---

```

Start
1: import libraries
2: Input
3: MI dataset
4: Output
5: Localization estimation accuracy
6: Start
7: ➔ specify the variable to be predicted
8: ➔ x1 = drop that variable from the data array
9: Model making
10: ➔ x_train, x_test, ytrain, ytest = sklearn.model_selection.train and test ()
11: ➔ linear = model.lineraregression()
12: Make model pickle
13: ➔ 1st dependent variable
14: ➔ ➔ pickle.dump()
15: ➔ 2nd dependent variable
16: ➔ ➔ pickle.dump()
17: ➔ 3rd dependent variable
18: ➔ ➔ pickle.dump()
19: ➔ 4th dependent variable
20: ➔ ➔ pickle.dump()
21: Load pickle
22: ➔ pickle = pickle. Load of (1st dependent variable)
23: ➔
24: pickle = pickle. Load of (2nd dependent variable)
25: ➔ pickle = pickle. Load of (3rd dependent variable)
26: ➔ pickle = pickle. Load of (4th dependent variable)
27: print the prediction
28: End

```

---

A linear regression model was called from the tensor flow to make the model for the prediction of our localization accuracy. In this particular study, we get an accuracy of between 95% and 97%. The small variations in the accuracy of every model are dependent on separate dependent variables of the datasets. We made a pickle of each model and stored it with the best accuracy, than for predicting the accuracy of certain cases, we called that specific model and found the accuracy of a specific combination of Tx and Rx nodes we wanted. For example, estimating the localization accuracy of the sensor Rx node when two anchor Tx nodes are deployed is one case, for three Tx nodes, it is the second case, four Tx nodes is the third case, and the deployment of eight Tx nodes is the fourth case. At the end, we plotted the accuracy of the model against the original values that we provided while training the model.

In Figure 4, the predicted localization estimation (PLE) and original localization estimation (OLE) are shown on the same graph for each dependent variable. We also included the numerical values of both the OLE and the PLE in Table 4 for the better understanding of the reader.

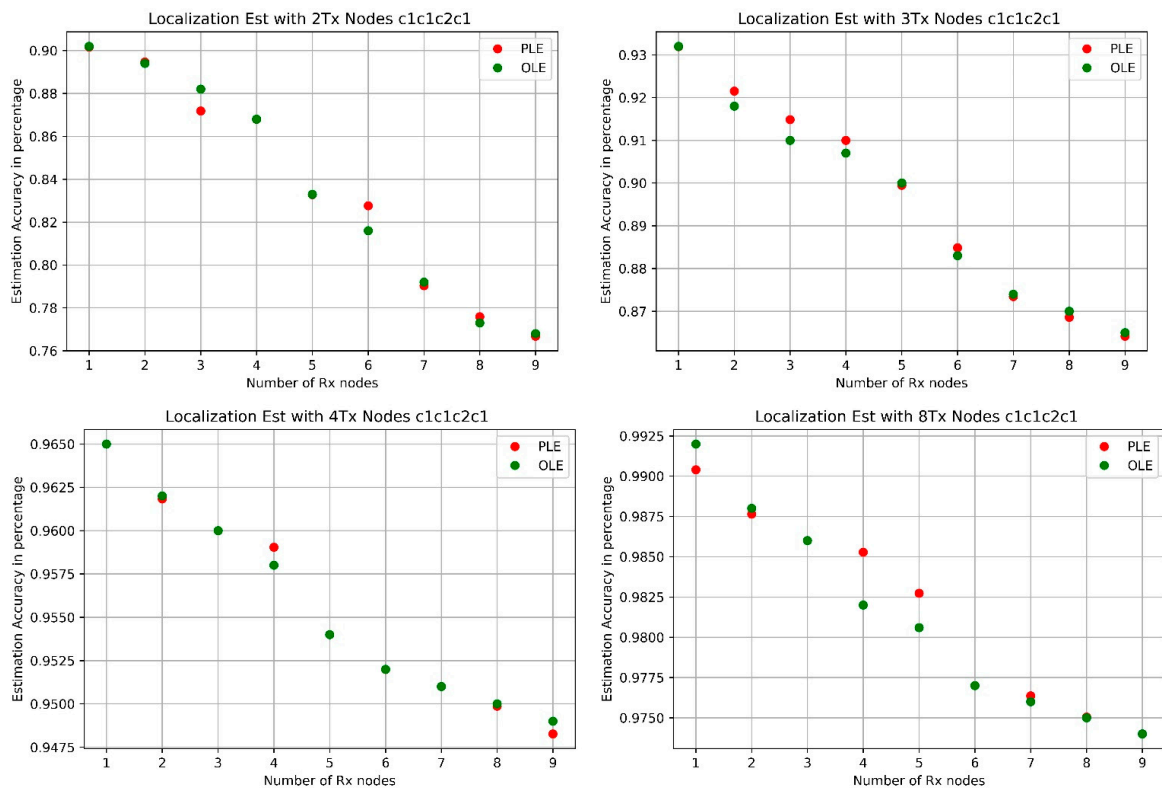


**Figure 4.** Predicting the localization estimation accuracy by considering c1c1c2c1.

#### 4.3. Prediction of Localization Accuracy for the c1c2, c2c2 Cases

A linear regression-based machine learning technique is used to predict the localization estimation accuracy of sensor Rx nodes while considering case 2 of both configurations 1 and 2, which are c1c2 and c2c2, respectively, shown in Figures 1c and 2c. The blind areas in the aforementioned figures are where no communication is taking place. As we can see that the blind areas of both configurations 1 and 2 are different, so is their effect on the accuracy of the localization estimation of the sensor Rx node. To display its effect in our prediction model, we have to tackle these different blind areas separately. This means here, in this scenario, we have eight dependent variables: four for c1c2 and four for c2c2.

The process of prediction as a pseudo code is shown as Algorithm 2. This whole process was done in python. As a first step, all the libraries regarding the procedure were loaded. Then, we loaded the data by which the model was first trained and validated, and then, the same data was used to test our model. We use 70/30 configuration, which means that 70 percent of the data was used to train and validate the model, and 30 percent of the data was used to test the model, as shown in Table 3. For the better understanding of the reader, the distribution of samples in the used MI dataset is, visualized in Figure 3, which is given above. A linear regression model is called from the tensor flow to make the model for the prediction of our localization accuracy estimation. Once the model is trained and validated, then we can test it with a small chunk of data to get the accuracy of the model. In this particular study, we get an accuracy of between 95% and 97%. The small variation in the accuracy of every model is dependent on separate dependent variables of the datasets. We made a pickle of each model and stored it with the best accuracy. Then, for predicting the accuracy of a certain case, we called that specific model and found the accuracy without even deploying sensor Rx nodes and anchor Tx nodes in the real world. For example, estimating the localization accuracy of the sensor Rx node when two anchor Tx nodes are deployed is one case, for three Tx nodes is the second case, four Tx nodes is third case, and the deployment of eight Tx nodes is the fourth case. At the end, we printed the accuracy of our model against the original values that we provided while training and validating the model.

**Table 4.** Original vs. predicted localization estimation accuracy results for case 1 of both configurations 1 and 2, i.e., c1c1 and c2c1.

S. No	Number of Tx Nodes	OLE 1 Rx Node	PLE 1 Rx Node	OLE2 Rx Node	PLE 2 Rx Node	OLE 3 Rx Node	PLE 3 Rx Node	OLE 4 Rx Node	PLE 4 Rx Node	OLE 5 Rx Node	PLE 5 Rx Node	OLE 6 Rx Node	PLE 6 Rx Node	OLE 7 Rx Node	PLE 7 Rx Node	OLE 8 Rx Node	PLE 8 Rx Node	OLE 9 Rx Node	PLE 9 Rx Node	OLE 10 Rx Node	PLE 10 Rx Node
1	2Tx nodes c1c1c2c1	90.2%	91.1%	89.4%	89.4%	88.2%	87.1%	86.8%	86.7%	83.3%	83.2%	81.6%	82.7%	80.5%	80.2%	79.2%	79.0%	77.3%	77.5%	76.8%	76.6
2	3Tx nodes c1c1c2c1	93.2%	93.1%	91.8%	92.1%	91%	90.9%	90.7%	91.4%	90%	89.9%	88.3%	88.4%	87.4%	87.3%	87%	86.8%	86.5%	86.4%	85.9%	85.7%
3	4Tx nodes c1c1c2c1	96.5%	96.4%	96.2%	96.1%	96%	96%	95.8%	95.9%	95.6%	95.7%	95.4%	95.4%	95.2%	95.1%	95.1%	95.0%	95%	94.9%	94.9%	94.8%
4	8Tx nodes c1c1c2c1	99.2%	99.0%	98.8%	98.7%	98.6%	98.6%	98.2%	98.5%	98.0%	98.2%	98.0%	97.9%	97.7%	97.7%	97.6%	97.6%	97.5%	97.5%	97.4%	97.4%

**Algorithm 2:** A Pseudo Code of the Prediction Process for c1c2c2c2.

---

```

Start
1:  import libraries
2:  Input
3:  MI dataset
4:  Output
5:  Localization estimation accuracy
6:  Start
7:  ➔      specify the variable to be predicted
8:  ➔
9:  x1 = drop that variable from the data array
10: Model making
11: ➔      x_train, x_test, ytrain, ytest = sklearn.model_selection.train and test ()
12: ➔      linear = model.lineraregression()
13: Make model pickle
14: ➔      1st dependent variable
15: ➔➔      pickle.dump()
16: ➔      2nd dependent variable
17: ➔➔      pickle.dump()
18: ➔      3rd dependent variable
19: ➔➔      pickle.dump()
20: ➔
21: 4th dependent variable
22: ➔➔      pickle.dump()
23: ➔      5th dependent variable
24: ➔➔
25: pickle.dump()
26: ➔      6th dependent variable
27: ➔➔      pickle.dump()
28: ➔
29: 7th dependent variable
30: ➔➔      pickle.dump()
31: ➔      8th dependent variable
32: ➔➔      pickle.dump()
33: Load pickle
34: ➔
35: pickle = pickle. Load of (1st dependent variable)
36: ➔      pickle = pickle. Load of (2nd dependent variable)
37: ➔      pickle = pickle. Load of (3rd dependent variable)
38: ➔      pickle = pickle. Load of (4th dependent variable)
39: ➔      pickle = pickle. Load of (5th dependent variable)
40: ➔      pickle = pickle. Load of (6th dependent variable)
41: ➔      pickle = pickle. Load of (7th dependent variable)
42: ➔      pickle = pickle. Load of (8th dependent variable)
43: print the prediction
44: End

```

---

In Figure 5, the predicted localization estimation (PLE) and original localization estimation (OLE) are shown on the same graph for each dependent variable. We also put the numerical values of both the OLE and the PLE in Table 5 for the better understanding of the reader.

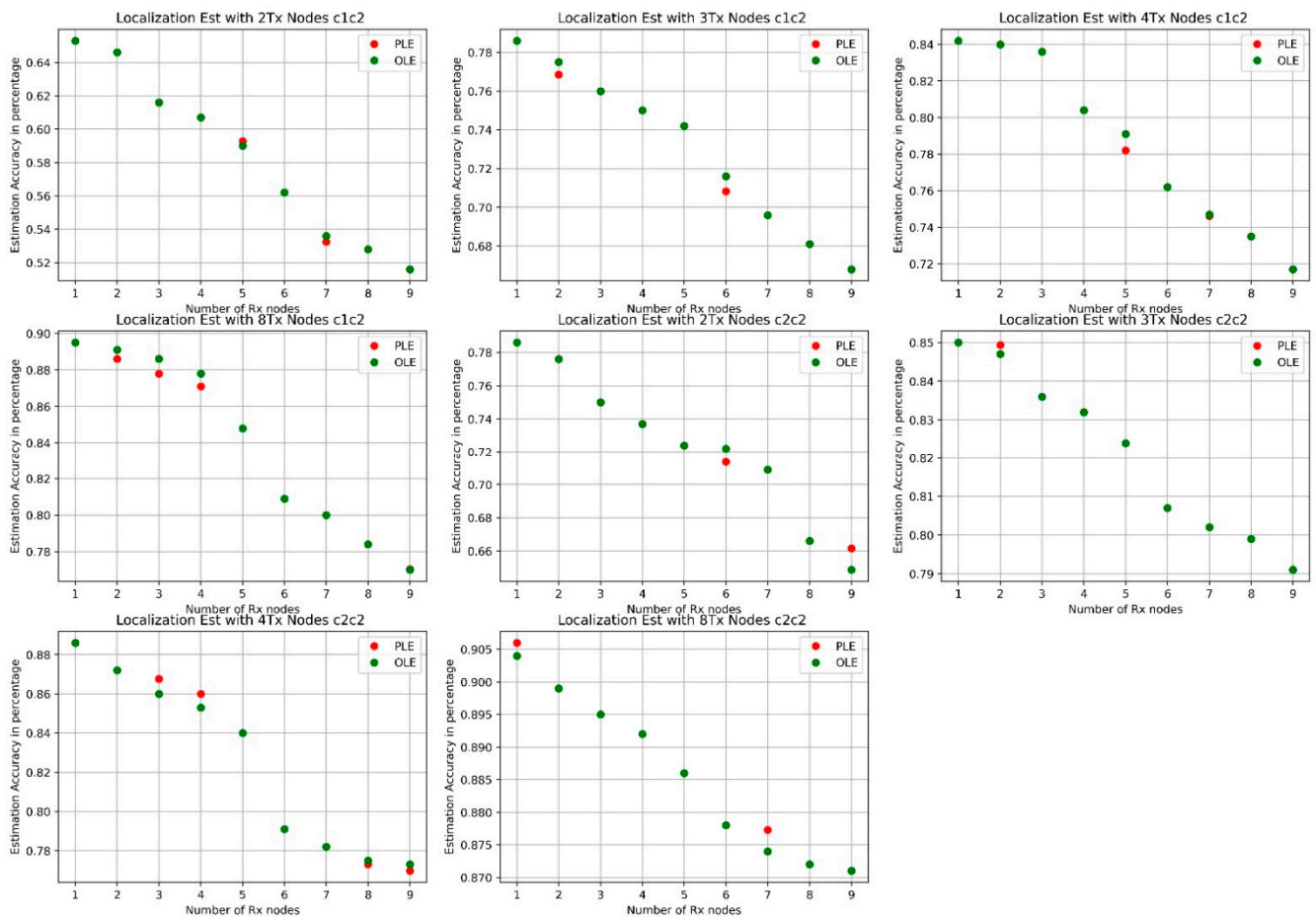


Figure 5. Predicting the localization estimation accuracy by considering c1c2c2c2.

Table 5. Original vs. predicted localization estimation accuracy results.

S.No	Number of Tx Nodes	Number of Rx Nodes																			
		OLE1 Rx Node	PLE 1 Rx Node	OLE2 Rx Node	PLE 2 Rx Node	OLE3 Rx Node	PLE 3 Rx Node	OLE4 Rx Node	PLE 4 Rx Node	OLE5 Rx Node	PLE 5 Rx Node	OLE6 Rx Node	PLE 6 Rx Node	OLE7 Rx Node	PLE 7 Rx Node	OLE8 Rx Node	PLE 8 Rx Node	OLE9 Rx Node	PLE 9 Rx Node	OLE10 Rx Node	PLE 10 Rx Node
1	2Tx nodes c1c2	65.3%	65.3%	64.5%	64.2%	61.6%	61.6%	60.7%	60.6%	59.0%	59.2%	56.2%	56.2%	53.6%	53.2%	52.8%	52.8%	52.2%	52.1%	51.6%	51.6%
2	2Tx nodes c2c2	78.6%	78.5%	77.6%	77.5%	76.2%	76.2%	75%	74.9%	73.7%	73.7%	72.5%	72.7%	72.2%	71.3%	70.9%	70.8%	66.6%	66.5%	64.8%	66.1%
3	3Tx nodes c1c2	77.4%	77.3%	77.5%	76.8%	76.8%	76.7%	76%	75.9%	75%	75%	74.2%	74.1%	71.6%	70.8%	69.6%	69.5%	68.1%	68.0%	66.8%	66.7%
4	3Tx nodes c2c2	85%	84.9%	84.7%	84.9%	83.6%	83.5%	83.2%	83.2%	82.4%	82.3%	81.6%	81.6%	80.7%	80.7%	80.2%	80.2%	79.9%	79.9%	79.7%	79.5%
5	4Tx nodes c1c2	84%	83.9%	84.2%	84.1%	83.6%	83.5%	80.4%	80.3%	79.1%	78.2%	76.2%	76.1%	74.7%	74.6%	73.5%	73.4%	72.6%	72.5%	72.1%	72.0%
6	4Tx nodes c2c2	88.6%	88.5%	87.2%	87.2%	86.5%	86.4%	85.3%	86.7%	84%	83.9%	82%	82%	79.1%	79.0%	78.2%	78.1%	77.5%	76.9%	77.3%	77.2%
7	8Tx nodes c1c2	89.5%	89.4%	89.1%	87.0%	88.6%	88.5%	87.8%	87.8%	84.8%	84.7%	82.9%	82.9%	80.9%	80.8%	79.1%	79.2%	78.4%	78.3%	77%	77%
8	8Tx nodes c2c2	90.4%	90.5%	90.1%	90.2%	89.5%	89.5%	89.2%	89.2%	88.6%	88.6%	88%	88%	87.8%	87.8%	87.4%	87.7%	87.2%	87.2%	87.1%	87.1%

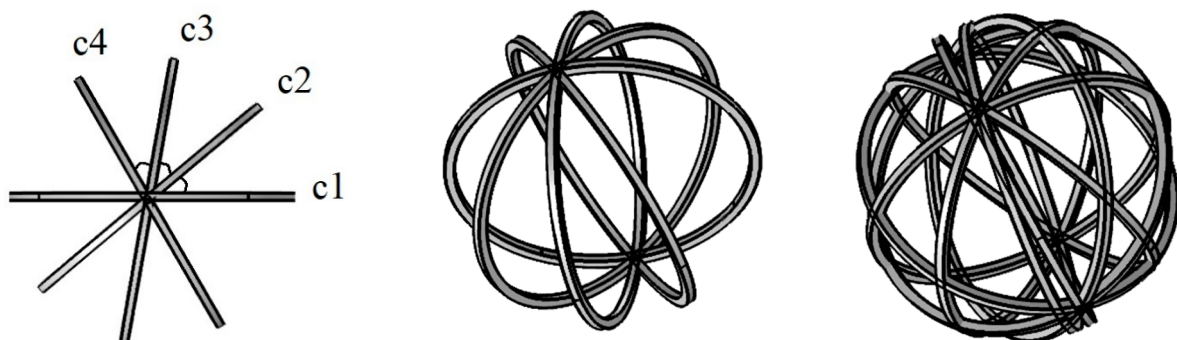
## 5. Design of Tri-Directional Coil for Omnidirectionality

A coil with blind areas limits the localization estimation accuracy. For the applications, which require high accuracy of node localization estimations in UWSNs, the localization error needs to be minimum. Therefore, it is critically important to keep the blind areas issue in mind while designing a TD coil. This section presents an improved design of a TD coil, which improves the magnetic flux pattern around the coil, with almost no blind areas and offers omnidirectionality.

### 5.1. Improving the Directivity Pattern

The results from our previous study [25], where we analyzed three different configurations of the applied excitation current, which generates two different patterns of magnetic flux around our opted MI TD coils, shown in Figures 1 and 2. Both of the generated magnetic flux patterns were further divided into cases for further analysis, where, in Figure 1, we observed blind areas from  $80^\circ$  to  $200^\circ$  and  $270^\circ$  to  $20^\circ$ , which, in total, combined to form  $120^\circ + 110^\circ = 230^\circ$  blind areas. In Figure 2, we observe blind areas from  $110^\circ$  to  $160^\circ$ ,  $210^\circ$  to  $260^\circ$ ,  $290^\circ$  to  $350^\circ$ , and  $20^\circ$  to  $70^\circ$ , which, in total, combined to form  $200^\circ$  of blind areas. These blind areas were causing a lot of inaccuracy in the localization of sensor Rx nodes in MI-UWSNs. The main point of concern due to these blind areas was that a lot of power source was wasted.

Additionally, we did not find any MI TD coil configuration by any research group in any study, where one can claim an omni directional magnetic flux or near to omni directional communication around the anchor Tx and sensor Rx coils. We in this study besides, a machine learning-based linear regression technique, to predict localization estimation accuracy in MI-UWSNs. However, had also focused on achieving an omni directional magnetic flux pattern around the MI TD coils. For which a combination of four coils approach at xy plane and an eight coils approach in xyz plane is opted to achieve almost near to omni directional magnetic flux pattern around the communicating coils in MI-UWSNs. The top view of the TD coil is shown in Figure 6a. Where c1 is denoting coil one, which is at  $0^\circ$ , c2 is denoting coil 2 which is at  $40^\circ$  from c1. c3 denotes coil 3, which is at  $80^\circ$  from c1 and  $40^\circ$  from c2. c4 denotes coil four which is at  $120^\circ$  from c1,  $80^\circ$  from c2 and  $40^\circ$  degree from c3. Do not confuse the aforementioned degrees as degree of computation of magnetic flux. Consider these degrees, as the degree of shift where the new coil will be placed. Which means that all the four coils are separate entities in itself and will have a computation degree of  $0^\circ$  to  $360^\circ$ . Figure 6b,c) are showcasing the side view of the opted MI TD coil in xy and xy, z planes, respectively.



(a) Top view of the TD coil for xy plane (b) 3D view of TD coil for xy plane (c) 3D view of TD coil for xy, z plane

**Figure 6.** A tridirectionally communicating four coil structure in xy plane and eight coil structure in the xy, z planes.

### The New Magneto Inductive Flux Pattern

The pseudo code to generate new flux pattern is given as Algorithm 3. So that one can regenerate the results portrayed in Figures 7–9. All these results are obtained in MATLAB.

Whereas a first step we have to find out the magneto motive force  $M$ . For which  $N$  is the number of turns,  $I$  is the excitation current applied,  $A$  is the area of the coil. Once this magneto motive force was found out, then we will find the magnetic flux produced by it. The magnetic flux produced by the magneto motive force will consists of two components. Both these components will be  $90^\circ$  out of phase to each other. We can call these components the major ( $H_x = \frac{M}{2\pi r^3} \cos\theta$ ) and minor ( $H_{x\tau} = \frac{M}{4\pi r^3} \sin\theta$ ) components. Major component is the one which is along the x axis and has a cos dependency. Minor component is the one which is tangent to the major axis and has a sin dependency. Once holding the plot of major and minor components of the generated magnetic flux on the same polar plot. We will highlight the maximum of both the aforementioned component. Next another coil with the same structural properties is introduced in the simulation environment but it will be  $40^\circ$  out of phase from the coil 1. Two more coils named, coil 3 and coil 4 with same structural properties and each one  $40^\circ$  out of phase from its previous coil are introduced in the simulation environment. Which provided us the magnetic flux pattern around the coil shown in Figure 7e. Next we had plotted the z component of the magnetic flux. For which the maximum of the xy plane will act as x axis and the z axis will be considered as y axis and the whole process will be repeated. Which will give us the magnetic flux pattern shown in Figure 8e. As we think that it will be difficult to assume the sketch of both the maximum values in 3D. So for the better understanding of the readers, we had plotted the maximum values of xy and xy, z plane in 3D that are shown in Figure 9a,b, respectively.

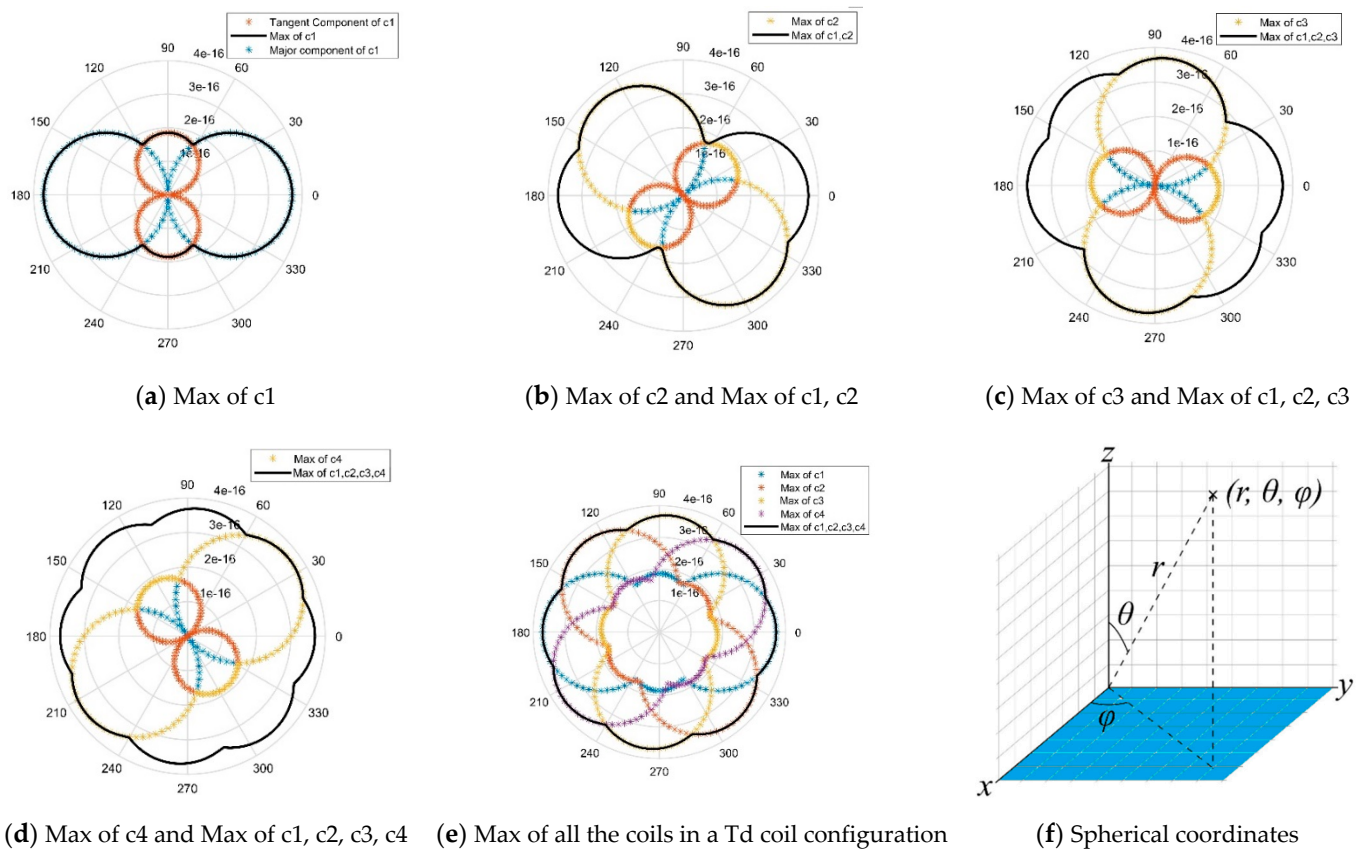


Figure 7. Max flux density of the magnetic fields and its directivity pattern calculated at xy plane.

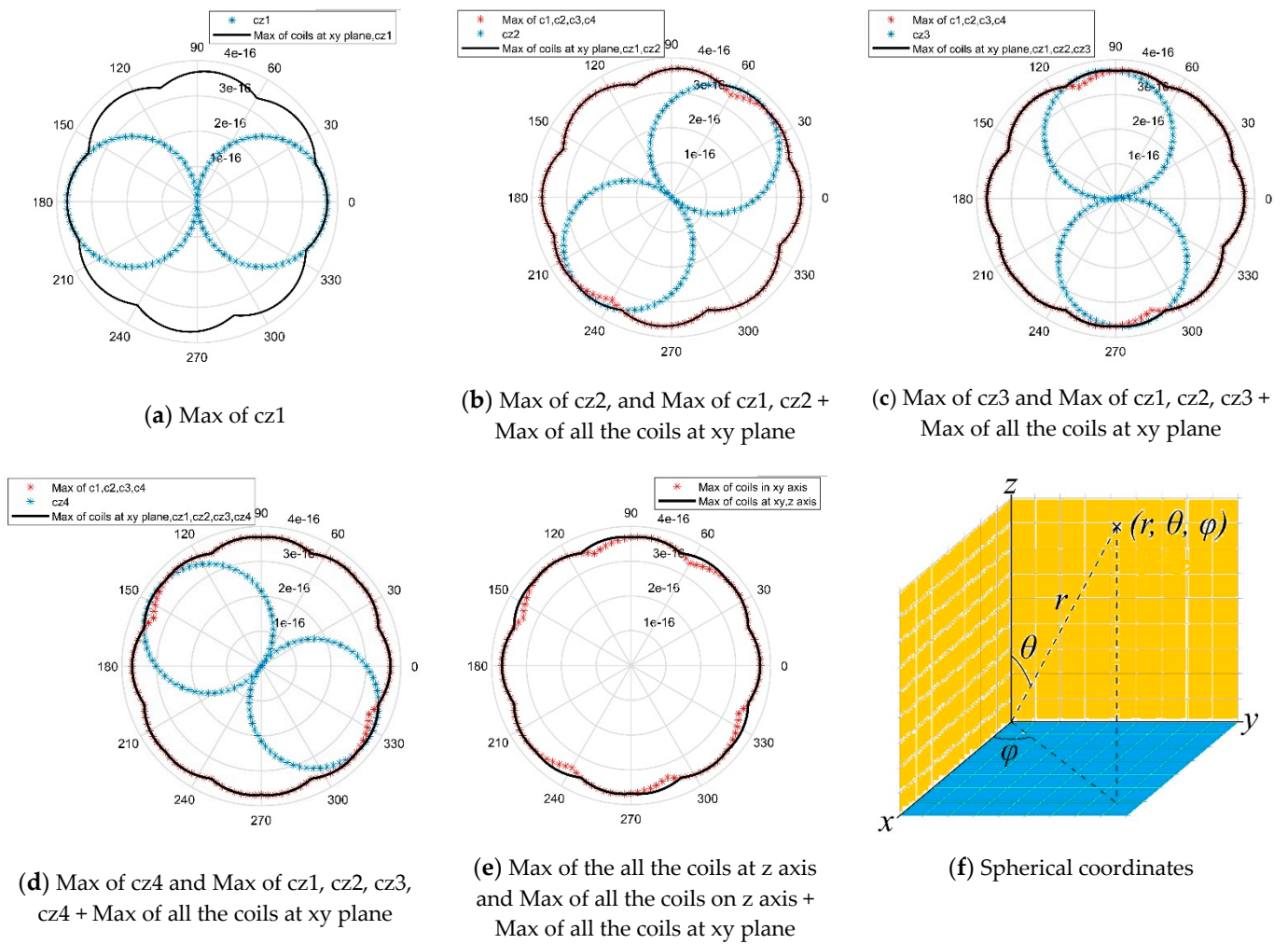


Figure 8. Max flux density of the magnetic fields and its directivity pattern calculated at  $xy, z$  plane.

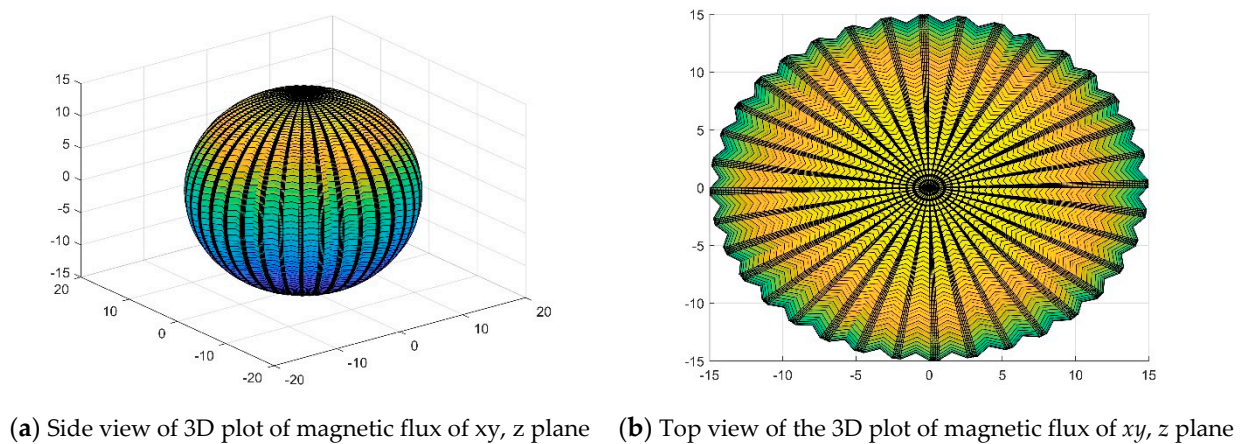


Figure 9. 3D plot of the maximum values of magnetic flux at  $xy$  and  $z$  plane.

When an excitation sinusoidal current is applied to  $c1$ . A magnetic flux around the coil is generated which can be found by  $M = NIA$ . Where  $M$  is the magneto motive force,  $N$  and  $A$  are number of turns and area of the communicating coils respectively. This generated magneto motive force consists of two parts. One is on the axis of communication at  $0^\circ$  and the other one is the tangential component which is normally  $90^\circ$  out of phase to the communicating axis.  $H_x = \frac{M}{2\pi r^3} \cos\theta$  is the calculation of major component of magnetic

flux density which is at  $0^\circ$ , and  $H_{x\tau} = \frac{M}{4\pi r^3} \sin\theta$  is the minor component of the generated magnetic flux around the communicating TD coil which is at  $90^\circ$ , and normally it is tangent to major component. In the aforementioned equations  $M$  is the magneto motive force,  $r$  is the distance, where the effect of magnetic flux can be observed. The cube on the distance in the equation indicates that the attenuation factor in MI communication is very high and the MI signal decays rapidly with respect to the increase in distance between Rx and Tx nodes. The magnetic flux pattern that can be seen in Figure 7a, shows both the major communicating component of the generated magnetic flux around the coil1 (c1) which is denoted with blue and is calculated by  $H_x = \frac{M}{2\pi r^3} \cos\theta$ . Whereas the tangential component of the generated magnetic flux around the c1, is denoted with orange and is calculated by  $H_{x\tau} = \frac{M}{4\pi r^3} \sin\theta$ . However, the black line, are the maximum values of the generated magnetic flux, which consist of both major and minor component of c1. The magnetic flux pattern shown in Figure 7b is obtained when another coil c2 is introduced Figure 6a. Which is at  $40^\circ$  shifted from the c1  $H_x = \frac{M}{2\pi r^3} \cos(\theta + 40)$  "see calculus one for graph shifting". Here the data denoted with yellow is the maximum of the major and minor components of c2. However, the black line, are the maximum values of the generated magnetic flux, which consist of both major and minor component of c1, c2.

Magnetic flux pattern shown in Figure 7c is obtained by introducing a 3rd coil c3, which is  $80^\circ$  shifted from c1  $H_x = \frac{M}{2\pi r^3} \cos(\theta + 80)$  and  $40^\circ$  shifted from c2 Figure 6a. Here the data denoted with yellow is the maximum of the major and minor components of c3. However, the black line, are the maximum values of the generated magnetic flux, which consist of both major and minor component of c1, c2 and c3. Magnetic flux pattern shown in Figure 7d is obtained by introducing a 4th coil c4, which is  $120^\circ$  shifted from c1  $H_x = \frac{M}{2\pi r^3} \cos(\theta + 120)$ ,  $80^\circ$  shifted from c2 and  $40^\circ$  shifted from c3 Figure 6a. Here the data denoted with yellow is the maximum of the major and minor components of c4. However, the black line, are the maximum values of the generated magnetic flux, which consist of both major and minor component of c1, c2, c3 and c4, where every next coil is  $40^\circ$  shifted in comparison to previous coil. In the next Figure 7e we have combined all the maximum values of the generated magnetic flux around the coils c1, c2, c3, c4, and shown it on the same plot to depict that this is how the magnetic flux will be, when using this new novel MI-TD coil configuration. The explained coil configuration is for xy plane shown with blue color in Figure 7f. This Figure 7f is introduced for the better understanding of the reader. The xy plane is colored blue to indicate that we had achieved a communication pattern for xy plane and now we will introduce a z component to our existing structure of the MI-TD coil to make the generated magnetic flux near to omnidirectional.

The z component of the TD coil configuration is same as coil structure opted for xy plane shown in Figure 6b. So by combining it with the existing coil structure we get a coil structure shown in Figure 6c. When an excitation current is applied to the coil 1 on z axis called as cz1. We obtained a magnetic flux pattern shown in Figure 8a, where the blue data is the maximum of cz1's major component. The reason we are not showing its conventional minor component is, because the whole xy plane is tangent to z plane as can be seen in Figure 7f. So as xy is the tangential component and all of its values had been founded, discussed and displayed previously in Figure 7 in this same section. We will simply take the maximum of all the coils on xy plane as a tangential component of each coil present at z plane. Magnetic flux pattern shown in Figure 8b is obtained by introducing a 2nd coil cz2 which is at  $40^\circ$  shifted from cz1. The blue data is the maximum of cz2, red data is the maximum of all coils at xy plane, and the data shown with black is the maximum of all coils at xy plane and the maximum of two coil introduced in z plane, i.e., cz1, cz2. Magnetic flux pattern shown in Figure 8c is obtained by introducing a 3rd coil cz3 which is at  $80^\circ$  shifted from cz1 and  $40^\circ$  shifted from cz2. The blue data is the maximum of cz3, red data is the maximum of all coils at xy plane, and the data shown with black is the maximum of all coils at xy plane and the maximum of three coils introduced in z plane, that are cz1, cz2 and cz3. Magnetic flux pattern shown in Figure 8d is obtained by introducing a 4th coil cz4 which is at  $120^\circ$  shifted from cz1,  $80^\circ$  shifted from cz2 and  $40^\circ$  shifted from

cz3. The blue data is the maximum of cz4, red data is the maximum of all coils at xy plane, and the data shown with black is the maximum of all coils at xy plane and the maximum of four coils introduced in z plane, that are cz1, cz2, cz3 and cz4. In Figure 8e we have plotted the maximum of all coils at xy plane shown with red, and the black line is showing the combination of both the maximum of all the coils at xy planes and maximum of all the coils at z planes. The Figure 8f is introduced for the better understanding of the reader. The xy plane is colored blue to indicate that we achieved a communication pattern for xy plane, and the z plane is colored yellow to indicate that magnetic flux pattern for z axis is also obtained.

---

**Algorithm 3:** A Pseudo Code for the Generation of Magnetic Flux Pattern.

---

**Start**

```

1:  Inputs
2:  N = number of turns
3:  I = current applied
4:  A = area of the coil
5:  M = NIA magneto motive force
6:  theta = 0–360
7:  theta_rad = convert theta values to radian
8:  Outputs
9:  ➔  $H_x = \frac{M}{2\pi r^3} \cos\theta$  major component of magnetic flux of coil 1 in xy plane
10: ➔  $H_{x\tau} = \frac{M}{4\pi r^3} \sin\theta$  minor component of magnetic flux of coil 1 in xy plane
11:
12: Max of major and minor axis
13:
14: polar plot
15: ➔  $H_x = \frac{M}{2\pi r^3} \cos\theta$  major component of magnetic flux of coil 2 in xy plane
16: ➔  $H_{x\tau} = \frac{M}{4\pi r^3} \sin\theta$  minor component of magnetic flux of coil 2 in xy plane
17:
18: Max of major and minor axis
19:
20: polar plot
21: ➔  $H_x = \frac{M}{2\pi r^3} \cos\theta$  major component of magnetic flux of coil 3 in xy plane
22: ➔  $H_{x\tau} = \frac{M}{4\pi r^3} \sin\theta$  minor component of magnetic flux of coil 3 in xy plane
23:
24: Max of major and minor axis
25:
26: polar plot
27: ➔  $H_x = \frac{M}{2\pi r^3} \cos\theta$  major component of magnetic flux of coil 4 in xy plane
28: ➔  $H_{x\tau} = \frac{M}{4\pi r^3} \sin\theta$  minor component of magnetic flux of coil 4 in xy plane
29:
30: Max of major and minor axis
31:
32: polar plot
33:
34: max coil 1, coil 2, coil 3, coil 4 in xy plane
35:
36: polar plot
37: ➔➔  $H_x = \frac{M}{2\pi r^3} \cos\theta$  major component of magnetic flux of coil1 in xy, z plane
38:
39: max coil 1, coil 2, coil 3, coil 4 in xy plane
40:

```

---

**Algorithm 3:** *Cont.*


---

```

41: Max of coils at xy plane plus max of coil 1 at z plane
42:
43: polar plot
44:  $\Rightarrow\Rightarrow H_x = \frac{M}{2\pi r^3} \cos\theta$  major component of magnetic flux of coil 2 in xy, z plane
45:
46: max coil 1, coil 2, coil 3, coil 4 in xy plane
47:
48: Max of coils at xy plane plus max of coil 2 at z plane
49:
50: polar plot
51:  $\Rightarrow\Rightarrow H_x = \frac{M}{2\pi r^3} \cos\theta$  major component of magnetic flux of coil 3 in xy, z plane
52:
53: max coil 1, coil 2, coil 3, coil 4 in xy plane
54:
55: Max of coils at xy plane plus max of coil 3 at z plane
56:
57: polar plot
58:  $\Rightarrow\Rightarrow H_x = \frac{M}{2\pi r^3} \cos\theta$  major component of magnetic flux of coil 4 in xy, z plane
59:
60: max coil 1, coil 2, coil 3, coil 4 in xy plane
61:
62: Max of coils at xy plane plus max of coil 4 at z plane
63:
64: polar plot
65:
66: theta = max of all coils at xy plane
67:
68: phi = max of coils at xy plan and z plane
69:
70: mesh/surf
71:  $\Rightarrow\Rightarrow$  end
72:  $\Rightarrow$  end
73: end

```

---

Now, as both the major and minor component of magnetic flux of the opted MI TD coil for UWSNs are obtained, for xy and z plane. We had plotted those points in a 3D plot for the ease of understanding of the reader. The sphere shown in Figure 9a is obtained by plotting the maximum values of the magnetic flux patterns shown in Figure 8e. Whereas Figure 9b on the other hand is the top view of the 3D plot to give the reader a new perspective for understanding the magnetic flux around the MI TD coil.

### 5.2. Improved Localization Accuracy

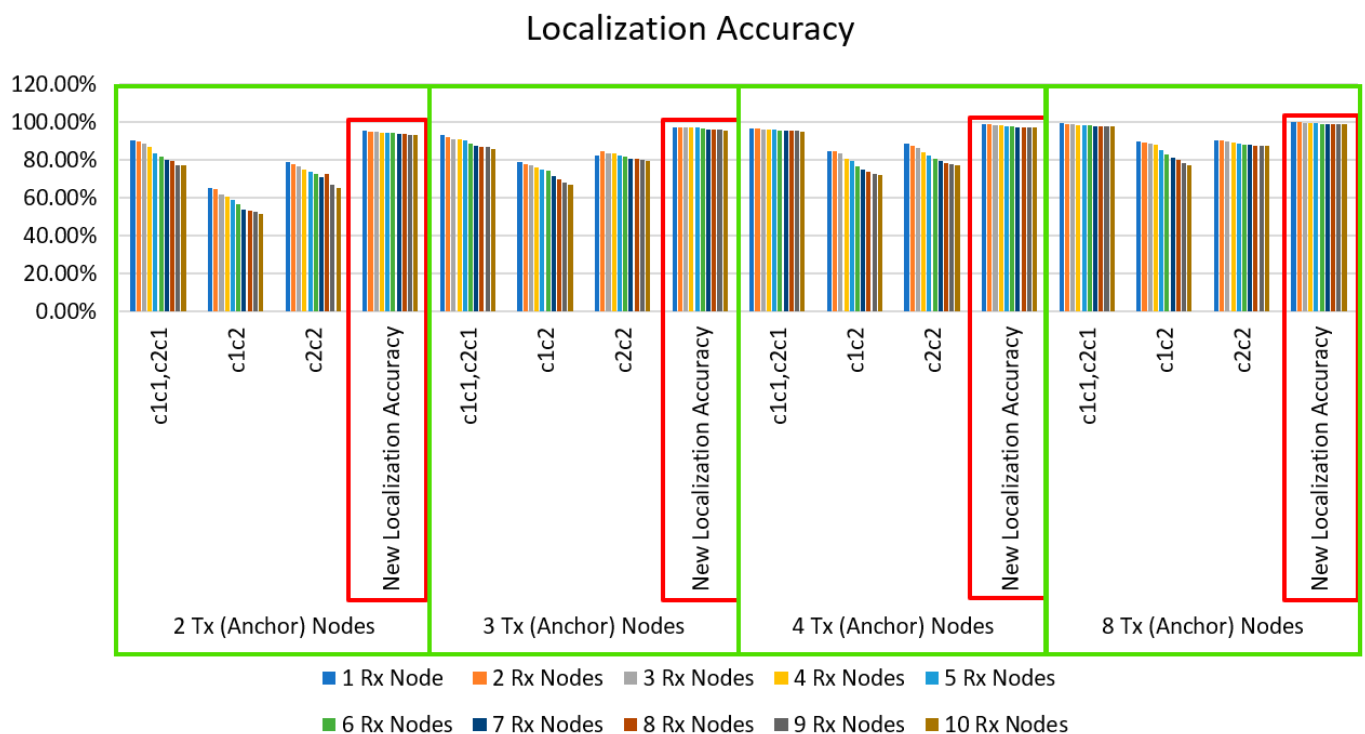
The localization accuracy shown of sensor Rx nodes in Table 1 for MI-UWSNs was low due to the presence of blind areas in the generated magnetic flux around the TD coils. The causes behind the blind areas, as well as the localization results, are discussed/analyzed in depth in our prior paper [25]. But now, as we had achieved almost omni directional pattern of magnetic flux by opting a new MI TD coil configuration discussed in Section 5. We had repeated the whole localization process for this newly obtained directivity patterns shown in Figure 7e and 8e and had obtained new localization accuracies shown in Table 6.

**Table 6.** New localization accuracy of sensor Rx nodes.

S. No	Number of Tx Nodes	1Rx Node	2Rx Node	3Rx Node	4Rx Node	5Rx Node	6Rx Node	7Rx Node	8Rx Node	9Rx Node	10Rx Node
1	2 Tx Nodes	95.23%	95.01%	94.86%	94.35%	94.03%	93.89%	93.75%	93.47%	93.12%	92.81%
2	3 Tx Nodes	97.21%	97.11%	97.02%	96.96%	96.75%	96.31%	96.07%	95.91%	95.75%	95.31%
3	4 Tx Nodes	98.75%	98.57%	98.21%	97.91%	97.75%	97.45%	97.02%	96.95%	96.87%	96.75%
4	8 Tx Nodes	99.75%	99.61%	99.47%	99.31%	99.18%	99.01%	98.91%	98.85%	98.71%	98.57%

## 6. Comparison and Summary of Old and Improved Localization Accuracy

The comparison of localization accuracies can be observed through a bar graph in Figure 10. Where we can see that our new localization accuracy does not contain any cases. That's because the newly opted MI TD coil design shown in Figure 6c and explained in Section 5, provides almost an omni directional magnetic flux around the coil shown in Figures 8e and 9a. We can see that localization accuracy of our previous configurations and its cases, i.e., C\_1C\_1, C\_2C\_1, C\_1C\_2 and C\_2C\_2 drops, as the number of sensor Rx nodes that are to be localized got increased. The results show that increasing the number of anchor Tx nodes from two to eight improved the localization estimation accuracy from 65.3 to 89.53% in case C\_1C\_1 and from 78.6 to 90.04% in case C\_2C\_1. However, as the number of sensor Rx nodes was increased from 1 to 10, the accuracy of localization estimation decreased from 89.53 to 77.06% for case C\_1C\_2, and from 90.04 to 87.13% for case C\_2C\_2. Whereas the new localization estimation accuracy is almost constant for the changing number of Tx and Rx nodes, i.e., when 2Tx nodes are used for localization, the accuracy decreases from 95.23 to 92.81%, for 3Tx nodes the accuracy decreases from 97.21 to 95.31%, for 4Tx nodes the accuracy decreases from 98.75 to 96.75% and for 8Tx nodes the accuracy decreases from 99.75 to 98.57%.

**Figure 10.** A comparative bar graph to elaborate/analyze the difference in localization accuracy.

## 7. Conclusions

A machine learning-based prediction of the localization-estimation accuracy of sensor Rx nodes in MI-UWSNs has been presented in this paper. The localization estimation plays

indispensable role in the performance of the MI-UWSNs, especially for IIoT applications. The created linear regression model presented accuracy between 95% and 97% for the presented cases. Furthermore, to address the problems of communication in the blind areas, a novel assembling configuration of TD coils has been proposed. This design generated a magnetic flux pattern that cover the blind areas present in the traditional designs. Due to this, the localization accuracy of our opted algorithm increased, which resulted in the achievement of an approximate omnidirectional MI communication. Moreover, the proposed design helps the MI-UWSNs to achieve better localization accuracy with less resources, i.e., the deployment of anchor Tx nodes. Due to this, localization can be done with a lesser number of anchor nodes, resulting in less energy consumption, which is critically important for IIoT applications. For future work, we suggest the prediction of omnidirectional flux values of H<sub>x</sub>, H<sub>y</sub> and H<sub>z</sub> through machine learning techniques, so that the accumulative magneto motive force can be predicted without even actually deploying resources. The Key outcomes of this article are:

- A MI dataset is created after extensive experimentation, which was previously not present on any forum up to our knowledge. This dataset that we had created and utilized, can be acquired with a proper institute to institute permission from the supervisor of the project Prof Qiao Gang.
- A machine learning-based linear regression method was used to automate the process of prediction of the location estimation accuracy in MI-UWSNs. Our model achieved an accuracy between 95 to 97%.
- A novel MI-TD coil design was presented which helps to improve the accuracy of the localization estimation from 87.13 to 98.57%.

**Author Contributions:** Conceptualization: Q.G. and A.M.; methodology: Q.G. and A.M.; software: A.M.; validation: Q.G.; formal analysis: A.M. and Z.U.K.; investigation: Q.G.; resources: Q.G. and A.M.; data curation: A.M.; writing—original draft preparation: A.M.; writing—review and editing: A.M., M.S.K., F.A. and J.A.; supervision: Q.G.; project administration: Q.G.; funding acquisition: Q.G. All authors have read and agreed to the published version of the manuscript.

**Funding:** This work is supported by the College of Underwater Acoustics Engineering, Harbin Engineering University, Heilongjiang, Harbin, China, National Natural Science Foundation of China (NSFC) under grant no U1806201.

**Institutional Review Board Statement:** Not applicable.

**Informed Consent Statement:** Not applicable.

**Data Availability Statement:** The data presented in this study will be available on request from the corresponding author.

**Acknowledgments:** This research work is supported by the College of Underwater Acoustic Engineering, Harbin Engineering University, Harbin 150001, Heilongjiang, China.

**Conflicts of Interest:** The authors declare no conflict of interest.

## References

1. Lenka, R.K.; Kolhar, M.; Mohapatra, H.; Al-Turjman, F.; Altrjman, C. Cluster-Based Routing Protocol with Static Hub (CRPSH) for WSN-Assisted IoT Networks. *Sustainability* **2022**, *14*, 7304. [[CrossRef](#)]
2. Arshad, J.; Rehman, A.U.; Othman, M.T.B.; Ahmad, M.; Tariq, H.B.; Khalid, M.A.; Moosa, M.A.R.; Shafiq, M.; Hamam, H. Deployment of Wireless Sensor Network and IoT Platform to Implement an Intelligent Animal Monitoring System. *Sustainability* **2022**, *14*, 6249. [[CrossRef](#)]
3. Mazhar, M.S.; Saleem, Y.; Almogren, A.; Arshad, J.; Jaffery, M.H.; Rehman, A.U.; Shafiq, M.; Hamam, H. Forensic Analysis on Internet of Things (IoT) Device Using Machine-to-Machine (M2M) Framework. *Electronics* **2022**, *11*, 1126. [[CrossRef](#)]
4. Rehman, A.U.; Asif, R.M.; Tariq, R.; Javed, A. Gsm based solar automatic irrigation system using moisture, temperature and humidity sensors. In Proceedings of the 2017 International Conference on Engineering Technology and Technopreneurship (ICE2T), Kuala Lumpur, Malaysia, 18–20 September 2017; pp. 1–4.
5. Hamrita, T.K.; Tollner, E.; Schafer, R.L. Toward fulfilling the robotic farming vision: Advances in sensors and controllers for agricultural applications. *IEEE Trans. Ind. Appl.* **2000**, *36*, 1026–1032. [[CrossRef](#)]

6. Ahmad, I.; Rahman, T.; Zeb, A.; Khan, I.; Ullah, I.; Hamam, H.; Cheikhrouhou, O. Analysis of Security Attacks and Taxonomy in Underwater Wireless Sensor Networks. *Wirel. Commun. Mob. Comput.* **2021**, *2021*, 1444024. [[CrossRef](#)]
7. Jukan, A.; Masip-Bruin, X.; Amla, N. Smart computing and sensing technologies for animal welfare: A systematic review. *ACM Comput. Surv.* **2017**, *50*, 1–27. [[CrossRef](#)]
8. Kim, S.; Jeong, J.; Seo, S.G.; Im, S.; Lee, W.Y.; Jin, S.H. Remote recognition of moving behaviors for captive harbor seals using a smart-patch system via bluetooth communication. *Micromachines* **2021**, *12*, 267. [[CrossRef](#)]
9. Dodge, K.L.; Kukulya, A.L.; Burke, E.; Baumgartner, M.F. TurtleCam: A “smart” autonomous underwater vehicle for investigating behaviors and habitats of sea turtles. *Front. Mar. Sci.* **2018**, *5*, 90. [[CrossRef](#)]
10. Coutinho, R.W.; Boukerche, A.J.I.I.; Magazine, M. North atlantic right whales preservation: A new challenge for internet of underwater things and smart ocean-based systems. *IEEE Instrum. Meas. Mag.* **2021**, *24*, 61–67. [[CrossRef](#)]
11. Fattah, S.; Gani, A.; Ahmedy, I.; Idris, M.Y.I.; Targio Hashem, I.A. A survey on underwater wireless sensor networks: Requirements, taxonomy, recent Advances, and open research challenges. *Sensors* **2020**, *20*, 5393. [[CrossRef](#)]
12. Kumar, S.; Perry, A.; Moeller, C.; Skvoretz, D.; Ebbert, M.; Ostrom, R.; Bennett, S.; Czipott, P. Real-time tracking magnetic gradiometer for underwater mine detection. In Proceedings of the Oceans’ 04 MTS/IEEE Techno-Ocean’04 (IEEE Cat. No. 04CH37600), Kobe, Japan, 9–12 November 2004; pp. 874–878.
13. Kamalesh, S.; Kumar, P.G.; Nanoscience Team. Fuzzy based secure intrusion detection system for authentication in wireless sensor networks. *J. Comput. Theor. Nanosci.* **2017**, *14*, 2465–2472. [[CrossRef](#)]
14. Kemna, S.; Hamilton, M.J.; Hughes, D.T.; LePage, K.D. Adaptive autonomous underwater vehicles for littoral surveillance. *Intell. Serv. Robot.* **2011**, *4*, 245–258. [[CrossRef](#)]
15. Abrudan, T.E.; Kypris, O.; Trigoni, N.; Markham, A. Impact of rocks and minerals on underground magneto-inductive communication and localization. *IEEE Access* **2016**, *4*, 3999–4010. [[CrossRef](#)]
16. Abrudan, T.E.; Xiao, Z.; Markham, A.; Trigoni, N. Distortion rejecting magneto-inductive three-dimensional localization (MagLoc). *IEEE J. Sel. Areas Commun.* **2015**, *33*, 2404–2417. [[CrossRef](#)]
17. Abrudan, T.E.; Xiao, Z.; Markham, A.; Trigoni, N. Underground incrementally deployed magneto-inductive 3-D positioning network. *IEEE Trans. Geosci.* **2016**, *54*, 4376–4391. [[CrossRef](#)]
18. Salem, H.; Attiya, G.; El-Fishawy, N. Intelligent decision support system for breast cancer diagnosis by gene expression profiles. In Proceedings of the 2016 33rd National Radio Science Conference (NRSC), Aswan, Egypt, 22–25 February 2016; pp. 421–430.
19. Salem, H.; Kabeel, A.; El-Said, E.M.; Elzeki, O.M. Predictive modelling for solar power-driven hybrid desalination system using artificial neural network regression with Adam optimization. *Desalination* **2022**, *522*, 115411. [[CrossRef](#)]
20. Ahmed, N.; Radchenko, A.; Pommerenke, D.; Zheng, Y.R. Design and evaluation of low-cost and energy-efficient magneto-inductive sensor nodes for wireless sensor networks. *IEEE Syst. J.* **2018**, *13*, 1135–1144. [[CrossRef](#)]
21. Ahmed, N.; Hoyt, J.; Radchenko, A.; Pommerenke, D.; Zheng, Y.R. A multi-coil magneto-inductive transceiver for low-cost wireless sensor networks. In Proceedings of the 2014 Underwater Communications and Networking (UComms), Sestri Levante, Italy, 3–5 September 2014; pp. 1–5.
22. Gaoding, N.; Bousquet, J.-F. A compact magneto-inductive coil antenna design for underwater communications. In Proceedings of the International Conference on Underwater Networks & Systems, Halifax, CA, USA, 6–8 November 2017; pp. 1–5.
23. Qiao, G.; Muzzammil, M.; Ahmed, N.; Ullah, I. Experimental investigation of optimal relay position for magneto-inductive wireless sensor networks. *Sensors* **2020**, *20*, 2720. [[CrossRef](#)]
24. Bai, X.; Ahmed, N.; Liu, S.; Qiao, G.; Li, H. Design of a Smart Relaying Scheme for Magneto Inductive Wireless Sensor Networks. In Proceedings of the Global Oceans 2020: Singapore–US Gulf Coast, Singapore, 5–14 October 2020; pp. 1–5.
25. Qiao, G.; Muhammad, A.; Muzzammil, M.; Shoaib Khan, M.; Tariq, M.O.; Khan, M.S. Addressing the Directionality Challenge through RSSI-Based Multilateration Technique, to Localize Nodes in Underwater WSNs by Using Magneto-Inductive Communication. *J. Mar. Sci. Eng.* **2022**, *10*, 530. [[CrossRef](#)]
26. Singh, A.; Kotiyal, V.; Sharma, S.; Nagar, J.; Lee, C.-C. A machine learning approach to predict the average localization error with applications to wireless sensor networks. *IEEE Access* **2020**, *8*, 208253–208263. [[CrossRef](#)]
27. Rauchenstein, L.T.; Vishnu, A.; Li, X.; Deng, Z.D. Improving underwater localization accuracy with machine learning. *Rev. Sci. Instrum.* **2018**, *89*, 074902. [[CrossRef](#)]
28. Gong, Z.; Li, C.; Jiang, F. A machine learning-based approach for auto-detection and localization of targets in underwater acoustic array networks. *IEEE Trans. Veh. Technol.* **2020**, *69*, 15857–15866. [[CrossRef](#)]
29. Chen, Q.Z.; Chen, Y.Z.; Fan, C.L.; Yang, F.; Wang, P.; Lei, Y.J. Research on Node Localization Algorithm in WSN basing Machine Learning. In *Advanced Materials Research*; Trans Tech Publications: Kapellweg, Switzerland, 2013; pp. 3568–3573.
30. Morgan, H. A fundamental equator point from observations of the sun, moon and planets 1894–1930. *Astron. J.* **1933**, *42*, 149–151. [[CrossRef](#)]
31. Fricke, W. Determination of the Equinox and Equator of the FK5. *Astron. Astrophys.* **1982**, *107*, L13–L16.
32. Chandrasekhar, V.; Seah, W. An area localization scheme for underwater sensor networks. In Proceedings of the OCEANS 2006—Asia Pacific, Singapore, 18–21 September 2006; pp. 1–8.
33. Li, X.; Deng, Z.D.; Rauchenstein, L.T.; Carlson, T.J. Contributed Review: Source-localization algorithms and applications using time of arrival and time difference of arrival measurements. *Rev. Sci. Instrum.* **2016**, *87*, 041502. [[CrossRef](#)]

34. Shi, X.; Wu, J. To hide private position information in localization using time difference of arrival. *IEEE Trans. Signal Process.* **2018**, *66*, 4946–4956. [[CrossRef](#)]
35. Yamamoto, R.; Matsutani, H.; Matsuki, H.; Oono, T.; Ohtsuka, H. Position location technologies using signal strength in cellular systems. In Proceedings of the IEEE VTS 53rd Vehicular Technology Conference, Spring 2001. Proceedings (Cat. No. 01CH37202), Rhodes, Greece, 6–9 May 2001; pp. 2570–2574.
36. Lin, D.-B.; Juang, R.-T. Mobile location estimation based on differences of signal attenuations for GSM systems. *IEEE Trans. Veh. Technol.* **2005**, *54*, 1447–1454. [[CrossRef](#)]
37. Hekimian-Williams, C.; Grant, B.; Liu, X.; Zhang, Z.; Kumar, P. Accurate localization of RFID tags using phase difference. In Proceedings of the 2010 IEEE International Conference on RFID (IEEE RFID 2010), Orlando, FL, USA, 14–16 April 2010; pp. 89–96.
38. Garg, V.; Jhamb, M. A review of wireless sensor network on localization techniques. *Int. J. Eng. Trends Technol.* **2013**, *4*, 1049–1053.
39. Aman, M.; Qiao, G.; Muzzammil, M. Design and Analysis of Li-fi Underwater Wireless Communication System. In Proceedings of the 2021 OES China Ocean Acoustics (COA), Harbin, China, 18–22 July 2021; pp. 1100–1103.
40. Aman, M.; Gang, Q.; Mian, S.; Muzzammil, M.; Tariq, M.O.; Khan, M.S. RSSI based Trilateration Technique to Localize Nodes in Underwater Wireless Sensor Networks through Optical Communication. In Proceedings of the 2021 16th International Conference on Emerging Technologies (ICET), Islamabad, Pakistan, 22–23 December 2021; pp. 1–5.
41. Sojdehei, J.J.; Wrathall, P.N.; Dinn, D.F. Magneto-inductive (MI) communications. In Proceedings of the MTS/IEEE Oceans 2001. An Ocean Odyssey. Conference Proceedings (IEEE Cat. No. 01CH37295), Honolulu, HI, USA, 5–8 November 2001; pp. 513–519.
42. Aman, M.; Gang, Q.; Durrani, M.A.; Muzzammil, M. Comparative Analysis of Magnetic Induction and Optical based Localization for Underwater Wireless Sensor Networks. In Proceedings of the 2021 International Conference on Frontiers of Information Technology (FIT), Islamabad, Pakistan, 12–13 December 2021; pp. 61–65.